Journal of Al-Farabi for Engineering Sciences (JFES)
Vol. 5, No. 1, 2026, **pp**. 51–65
ISSN: 2617-5517 | **DOI**: https://doi.org/10.59746/byt32350

Leakage-Free Segmentation-Based ANN for Crack Localization and Depth Estimation in Cantilever Beams

Mohammad Majeed[1,*], Khaldoon Brethee[2], Firas Basim[3, 4, 5]
[1] Department of Mechanical Engineering, Faculty of Engineering, University of Anbar, Ramadi 31001, Iraq. Email: moh24e2002@uoanbar.edu.iq
[2] Department of Mechanical Engineering, Faculty of Engineering, University of Anbar, Ramadi 31001, Iraq. Email: khaldon77m@uoanbar.edu.iq
[3] Smart Power Generation Research Centre, College of Engineering, Universit Tenaga Nasional (UNITEN), Kajang 43000, Malaysia.
[4] *Faculty of Engineering, Sohar University, P.O. Box 44, Sohar PCI 311, Oman.*
[5] Engineering College, Al-Bayan University, Baghdad, Iraq. Email: firas@uniten.edu.my

Received 05/01/2026, Revised 8/3/2026, Accepted 30/4/2026

Abstract: This study develops a controlled and leakage-free learning framework for vibration-based crack characterization in a metallic cantilever beam using compact relative frequency shift (RFS) features. A fully numerical methodology is implemented in MATLAB based on a one-dimensional Euler–Bernoulli finite-element model, in which the cracked beam element is represented through a local stiffness matrix and statically condensed into an equivalent element for global assembly. A database of 1200 labelled damaged scenarios is generated by varying crack location over 100 beam elements and crack depth over 12 levels from 0.20 to 2.40 mm. Each scenario is represented by a six-dimensional RFS vector computed from the first six bending natural frequencies, while the outputs are the normalized crack location and crack-depth ratio. All models are trained and evaluated under a single leakage-free Master Split (70/15/15) to ensure fair and reproducible comparison. The baseline artificial neural network achieves test-set mean absolute errors of 2.992 mm for crack location and 0.0251 mm for crack depth. Under the same split, a segmentation-based coarse-to-fine strategy reduces these errors to 1.245 mm and 0.0211 mm, respectively. The main contribution of this work is a reproducible leakage-free segmentation-based ANN framework that improves RFS-based crack localization and depth estimation within a controlled numerical setting.

Keywords: Structural health monitoring, cantilever beams, relative frequency shift, crack localization, crack depth estimation, artificial neural networks.

1. Introduction

Structural cracks in beam-like components can reduce stiffness and, if left undetected, may compromise structural safety and lead to severe failure [1], [2]. Structural Health Monitoring (SHM), therefore, seeks reliable, repeatable approaches to detect damage at an early stage and to support condition-based maintenance rather than purely time-based inspection [3], [4]. Among SHM approaches, vibration-based methods remain attractive because damage-related stiffness changes influence the structure's measured dynamic response, leading to changes in modal properties such as natural frequencies and mode shapes, and to variations in frequency-response characteristics [1], [5]. In practice, however, converting such response changes into reliable indicators for damage detection, localization, and quantification remains challenging because of measurement noise, operational and environmental influences, and uncertainties in the reference baseline state [4], [5]. Accordingly, robust vibration-based damage characterization requires carefully selected features and well-controlled evaluation frameworks.

Classical vibration-based crack diagnosis has commonly relied on features derived from damage-induced changes in modal parameters, including natural frequencies, mode shapes, and their curvature-based forms [6], [7], [8]. Natural-frequency-based descriptors, including relative frequency shifts, are particularly attractive because natural frequencies are among the easiest modal quantities to estimate, can often be obtained using relatively inexpensive and robust instrumentation, and generally require fewer sensors than mode-shape-based methods [6]. By contrast, curvature- or derivative-based indicators may be sensitive to measurement noise and to the spatial resolution of the measured mode shapes, and their localization capability may

deteriorate near boundaries or in regions where curvature approaches zero, leading to smeared or ambiguous damage indications [5], [9], [10]. In addition, many such formulations assume the availability of an intact baseline structure, an assumption that may not hold in many practical or in-situ applications [5], [10]. These limitations motivate the use of compact relative frequency shift (RFS) features within learning-based models such as RF and artificial neural networks (ANNs) to estimate crack location and severity directly from vibration-derived information [6]. Frequency changes are also often regarded as relatively less noise-contaminated features for damage identification [11]. For these reasons, compact frequency-based representations, particularly RFS vectors, provide a practically attractive basis for direct learning-based crack inference.

In recent years, data-driven methods, including machine learning and fuzzy inference systems, have been increasingly applied to estimate crack location and depth or severity from vibration-derived information [1], [2], [12]. Artificial neural networks (ANNs), in particular, have been widely used in vibration-based damage identification because they can learn the relationship between vibration-derived features, such as modal parameters, and damage-related outputs after training [1], [12]. Depending on the diagnostic objective, this learning task may be formulated either as classification of damage states or as regression of damage-related quantities [1]. However, the reported effectiveness of such models depends not only on the learning algorithm itself, but also on the choice of input features, the definition of the targets, and the rigor of the evaluation protocol.

A persistent limitation in supervised learning-based SHM is the lack of sufficiently rich and representative labeled data covering diverse damage scenarios and operating conditions, which constrains robust model development and validation [13], [14], [15]. For this reason, simulation-based strategies and digital-twin-oriented modeling are increasingly used to generate controlled datasets for learning-based damage inference, especially when large-scale experimental measurements are difficult or costly to obtain [13], [14], [16]. The usefulness of such numerically generated datasets, however, depends on how consistently the simulated scenarios, extracted features, and learning targets are defined.

Against this background, the present study develops a fully numerical, simulation-based learning framework for crack characterization in a metallic cantilever beam using vibration-derived features and supervised learning. The framework takes frequency-derived features as inputs and predicts crack location and crack depth as outputs. A unified finite-element modelling basis is used to generate a consistent labelled dataset, in line with simulation-assisted and digital-twin-assisted data-generation strategies reported in the SHM literature [14], [17]. To ensure fair and reproducible evaluation, model training, validation, and testing are conducted under a strictly leakage-free protocol. The resulting framework is frequency-based and uses a compact multi-mode feature vector constructed from relative changes in natural frequencies (RFS), consistent with prior learning-based studies that utilize modal-parameter information for damage identification in beam-like structures [6], [18].

In this work, the proposed framework is evaluated in a fully numerical, noise-free setting to establish a controlled baseline under consistent conditions. In addition, literature-reported experimental RFS values are used as external consistency check for the proposed RFS-based inference. Robustness to measurement noise and to operational or environmental variability lies outside the scope of the present numerical baseline and is therefore left for future experimental investigation. Although the coarse-to-fine segmentation concept adopted in this study is motivated by the approach reported in [6], the novelty of the present work does not lie in introducing segmentation itself. Rather, it lies in integrating the segment-wise ANN models into a unified leakage-free inference and evaluation framework. In the proposed implementation, the true crack location is used only to define segment membership during training, not to select the segment

during final testing. During inference, the overall ANN first provides a coarse crack-location estimate, this estimate is then used to select the relevant segment-specific ANN, and the selected segment model provides the final refined prediction. Accordingly, the segmented framework is evaluated as a single overall predictor over the complete test set under the same Master Split used for the baseline ANN. This enables a direct and fair comparison between the baseline and segmentation-based ANN models while reducing the risk of information leakage or split-induced bias. The main contributions of this work are:

- A unified simulation-based framework for a metallic cantilever beam to generate labelled vibration datasets for crack location and crack depth estimation.
- A compact RFS-based feature framework for direct crack characterization using multi-mode relative frequency information.
- A unified leakage-free segmentation-based inference protocol in which the segment-wise ANN models are integrated into a single overall predictor, with final segment selection driven by the coarse output of the overall ANN rather than by the true crack location.

2. Method

2.1. Numerical model of the cantilever beam

This study is conducted in a fully numerical setting within MATLAB, relying on a one-dimensional Euler–Bernoulli finite element (FE) formulation for a prismatic cantilever beam. The model employs two degrees of freedom per node: the transverse displacement v and the cross-sectional rotation θ. The beam geometry is defined as $L = 1.0$ m, $b = 0.05$ m, and $h = 0.005$ m. A steel-like material is assumed with $E = 2.1 \times 10^{11}$ Pa, $\rho = 7850$ kg/m^3, and $\nu = 0.3$.

A mesh of $N_e = 100$ Euler–Bernoulli elements is adopted. For each scenario (healthy or damaged), free-vibration eigenvalue analysis is performed to extract the required bending natural frequencies and corresponding mode-shape information that supports feature construction.

2.2. Element-level crack representation (8×8 local stiffness matrix with condensation and hard displacement continuity)

To represent a single transverse crack within an Euler–Bernoulli beam element, the cracked element is constructed through a compact element-level procedure. First, the original beam element is divided into two half-elements, and an internal crack interface is introduced. Second, the crack flexibility is represented by a rotational spring between the two interface rotations, while transverse displacement continuity is enforced through a hard kinematic constraint. Third, the internal interface degrees of freedom are removed by static condensation, resulting in an equivalent 4×4 cracked-element stiffness matrix suitable for standard global assembly. This procedure preserves the physical interpretation of the crack model while keeping the final assembled FE model compatible with the conventional two-node Euler–Bernoulli beam formulation (Appendix A.6, Eq. (A.17)–(A.19)).[19]

2.2.1. Baseline Euler–Bernoulli element stiffness 4×4

For a standard Euler–Bernoulli beam element of length L, flexural rigidity EI, and nodal degrees of freedom $[v, \theta]$ at each node, the consistent bending stiffness matrix is

$$\mathbf{K}_e(EI, L) = \frac{EI}{L^3}\begin{bmatrix} 12 & 6L & -12 & 6L \\ 6L & 4L^2 & -6L & 2L^2 \\ -12 & -6L & 12 & -6L \\ 6L & 2L^2 & -6L & 4L^2 \end{bmatrix} \quad (1)$$

In the cracked-element construction. this matrix is used as the building block for each half-element by substituting $L = L_e/2$ (Sec. 10.3.2, Eq. (10.55)). [19]

2.2.2. Construction of the 8×8 cracked-element stiffness

An internal interface is introduced between the two half-elements, yielding four local nodes: left end (node 1), left interface (node 2), right interface (node 3), and right end (node 4). The local displacement vector is ordered as

$$q_e = [v_1, \theta_1, v_2, \theta_2, v_3, \theta_3, v_4, \theta_4]^T \quad (2)$$

where (v_2, θ_2) and (v_3, θ_3) denote the degrees of freedom immediately to the left and right of the crack interface, respectively.

First, the two half-element stiffness matrices $K_{1/2} = K_e(EI, L_e/2)$ are assembled into an uncoupled 8×8 block-diagonal matrix:

$$K_{blk} = \begin{bmatrix} K_{1/2} & 0 \\ 0 & K_{1/2} \end{bmatrix} \quad (3)$$

Second, crack compliance is introduced via a rotational spring that couples the interface rotations θ_2 and θ_3. This is implemented by augmenting the (θ_2, θ_3) sub-block as

$$\Delta k_\theta = k_\theta(\lambda) \begin{bmatrix} 1 & -1 \\ -1 & 1 \end{bmatrix}_{(\theta_2, \theta_3)}, \qquad \lambda = \frac{a}{h}, \quad (4)$$

where a is the crack depth and h is the beam thickness. The rotational spring stiffness is adopted from [20] and is expressed as

$$k_\theta(\lambda) = \frac{EI}{(1 - v^2) 6\pi h \emptyset(\lambda)}, \qquad \lambda = \frac{a}{h}. \quad (5.a)$$

with Poisson's ratio v, and the compliance function $\emptyset(\lambda)$ given by

$$\emptyset(\lambda) = 0.655563(0.9566 - 1.5944\lambda + 7.008\lambda^2 - 15.21\lambda^3 + 30.9534\lambda^4 - 50.38657\lambda^5 + 71.8488\lambda^6 - 62.1624\lambda^7 + 29.89486\lambda^{10}) \quad (5.b)$$

To avoid numerical singularities for very small λ, lower bounds are applied in implementation (e.g., $\lambda \geq 10^{-12}, \emptyset(\lambda) \geq 10^{-18}$).

Then we get

$$K_{lok} = K_{blk} + \Delta k_\theta \quad (6)$$

Third, displacement continuity at the interface is imposed as a hard constraint:

$$v_2 = v_3 \quad (7)$$

This constraint is enforced by merging the two displacement degrees of freedom into a single shared coordinate v_c. Defining the reduced generalized coordinates

$$q_r = [v_1, \theta_1, v_c, \theta_2, \theta_3, v_4, \theta_4]^T \in \mathbb{R}^7 \quad (8)$$

the original local vector is related to q_r by a linear mapping $q_e = Tq_r$, where the transformation matrix $T \in \mathbb{R}^{8\times7}$ is

$$T = \begin{bmatrix} 1 & 0 & 0 & 0 & 0 & 0 & 0 \\ 0 & 1 & 0 & 0 & 0 & 0 & 0 \\ 0 & 0 & 1 & 0 & 0 & 0 & 0 \\ 0 & 0 & 0 & 1 & 0 & 0 & 0 \\ 0 & 0 & 1 & 0 & 0 & 0 & 0 \\ 0 & 0 & 0 & 0 & 1 & 0 & 0 \\ 0 & 0 & 0 & 0 & 0 & 1 & 0 \\ 0 & 0 & 0 & 0 & 0 & 0 & 1 \end{bmatrix}. \quad (9)$$

Accordingly, after adding the rotational spring contribution, the reduced cracked-element stiffness matrix is obtained (Sec. 2.5, Eq. (2.50)). [19]

$$k_r = T^T K_{lok} T \in \mathbb{R}^{7\times7}. \quad (10)$$

2.2.3. Static condensation to an equivalent 4×4 element

For global assembly, the internal interface degrees of freedom are eliminated via static condensation to yield an equivalent 4×4 stiffness matrix that connects only the external end degrees of freedom $[v_1, \theta_1, v_4, \theta_4]$. The reduced coordinate vector is partitioned as

$$\mathbf{q_r^{ext}} = [\boldsymbol{v_1}, \boldsymbol{\theta_1}, \boldsymbol{v_4}, \boldsymbol{\theta_4}]^{\boldsymbol{T}}, \qquad \mathbf{q_r^{int}} = [\boldsymbol{v_c}, \boldsymbol{\theta_2}, \boldsymbol{\theta_3}]^{\boldsymbol{T}} \tag{11}$$

and the stiffness matrix $\mathrm{K_r}$ is correspondingly partitioned into blocks

$$\mathbf{K_r} = \begin{bmatrix} \mathbf{K_{ee}} & \mathbf{K_{ec}} \\ \mathbf{K_{ce}} & \mathbf{K_{cc}} \end{bmatrix}. \tag{12}$$

The condensed (effective) element stiffness used for global assembly is obtained by the Schur complement:

$$\mathbf{K_{eff}} = \mathbf{K_{ee}} - \mathbf{K_{ec}}\mathbf{K_{cc}^{-1}}\mathbf{K_{ce}} \in \mathbb{R}^{\mathbf{4\times 4}} \tag{13}$$

Consistent with the numerical implementation adopted in this study, the crack is assumed to affect the stiffness matrix only, while the element mass matrix remains unchanged (Appendix A.6, Eqs. (A.17)–(A.19)). [19]

2.3. Damage scenarios and dataset construction

A single-crack database is generated after computing the healthy baseline. Crack location is defined at the element level, allowing the crack to occur in any of the 100 elements (i.e., 100 possible locations along the span). Crack depth is discretized into 12 levels in millimeters, $a = \{0.20, 0.40, 0.60, \dots, 2.40\}$ mm, with a constant step of 0.20 mm. Consequently, the total number of simulated scenarios is $N = 100 \times 12 = 1200$. For compact representation, the non-dimensional location and severity are defined as $\xi_c = x_c/L$ and $\xi_c = a/h$. Although the FE computations are carried out in SI units, the learning targets are defined in non-dimensional form. For reporting and interpretation, the corresponding dimensional quantities in millimeters are obtained via $\hat{x}_{mm} = \mathrm{x}_c \times 10^3$ and $a_{mm} = \lambda h \times 10^3$.

2.4. Master split for unified and reproducible evaluation

To ensure a fair, unified, and fully reproducible evaluation, a single official "Master Split" is constructed over the complete dataset of $N = 1200$ simulated scenarios. Rather than relying on independent random partitions across different training stages, all models and all reported metrics are computed using the same Train/Validation/Test partition, thereby eliminating split-induced variability and enabling direct, like-for-like comparisons. The adopted partition is:

- Train: 840 samples (70%)
- Validation: 180 samples (15%)
- Test: 180 samples (15%)

A fixed official random seed,$\mathrm{masterSeed} = 2026$ is used to guarantee exact reproducibility.

In addition to the global split (overall-beam training), the same official split is projected onto a set of nine overlapping beam segments, generating segment-specific Train/Validation/Test indices while maintaining strict consistency with the global Master Split. This design supports both overall and segment-wise evaluation under an identical leakage-free protocol, ensuring that any performance differences reflect model behavior rather than differences in data partitioning. The resulting global split indices and the segment-projected indices are stored for full reproducibility and consistent downstream training/evaluation.

It should be noted that the Master Split used in this study is not intended to replace conventional cross-validation as a general estimator of model variability. Instead, it is adopted as a fixed comparison protocol to ensure that the baseline ANN, the overall ANN, and the segment-specific ANN models are trained, validated, and tested on mutually consistent samples. In this way,

the comparison between the baseline and segmentation-based strategies is not affected by different random partitions, fold-to-fold variability, or segment-wise data leakage. The main purpose of the Master Split is therefore to provide a reproducible and leakage-free basis for like-for-like comparison under the controlled numerical setting of this study.

2.5. Relative Frequency Shifts (RFS).

The first Six bending natural frequencies are extracted from the healthy baseline and from each damaged scenario. Let $i = 1, \dots, N$ index the damaged scenarios, where $N = 1200$ in this study. For mode r, the relative frequency shift (RFS) is defined following [21] as

$$\mathbf{RFS}_r^{(i)} = \mathbf{1} - \frac{\boldsymbol{f}_r^{\boldsymbol{D},(i)}}{\boldsymbol{f}_r^{\boldsymbol{H}}}, \qquad \boldsymbol{r} = \mathbf{1}, \dots, \mathbf{6}. \tag{14}$$

Where f_r^H and $f_r^{D,(i)}$ denote the r −th bending natural frequency of the healthy condition and the i −th damaged scenario, respectively.

To provide a qualitative visualization of how the relative frequency shift varies with crack location and severity, Figure 1 plots the RFS values for the first three bending modes as functions of the normalized crack location $\xi_c = x_c/L$ for three representative crack depths (a = 0.80, 1.60, and 2.40 mm). The results indicate that the RFS response is both mode-dependent and location-dependent, with an increased magnitude observed for larger crack depths under the studied numerical conditions. Although the learning model in this study uses the first six modes to construct the final RFS feature vector, modes 1–3 are shown here for clarity and to highlight the underlying sensitivity trends.

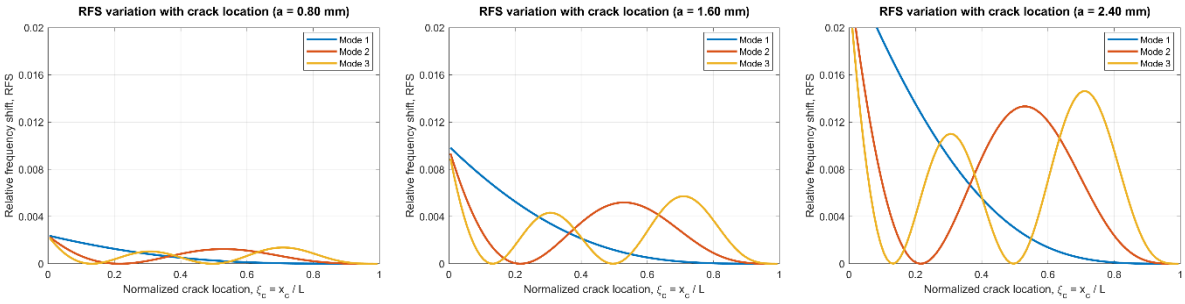

Figure 1. Relative Frequency Shift (RFS) versus normalized crack location $\xi_c = x_c/L$ for the first three bending modes (Modes 1–3), shown for three crack depths: (a) a =0.80 mm, (b) a = 1.60 mm, and (c) a =2.40 mm. The curves show that the RFS response is both mode-dependent and location-dependent, with larger crack depths producing higher RFS magnitudes under the studied numerical conditions. The reference case corresponds to element $e = 50$ ($\xi_c = 0.495$). Source: Authors' work (generated in MATLAB).

To further illustrate the adopted RFS feature representation, Figure 2 shows example "RFS fingerprints" for a fixed crack depth (a = 1.6 mm) at three representative crack locations along the cantilever span. Each fingerprint is the 6-dimensional vector $[RFS_1, RFS_2, \dots, RFS_6]$, where each component corresponds to one bending mode. These examples provide an intuitive visualization of how the multi-mode RFS signature varies with the crack position, consistent with the feature vector definition used for learning.

 ISSN: 2617-5517 | **DOI**: https://doi.org/10.59746/byt32350

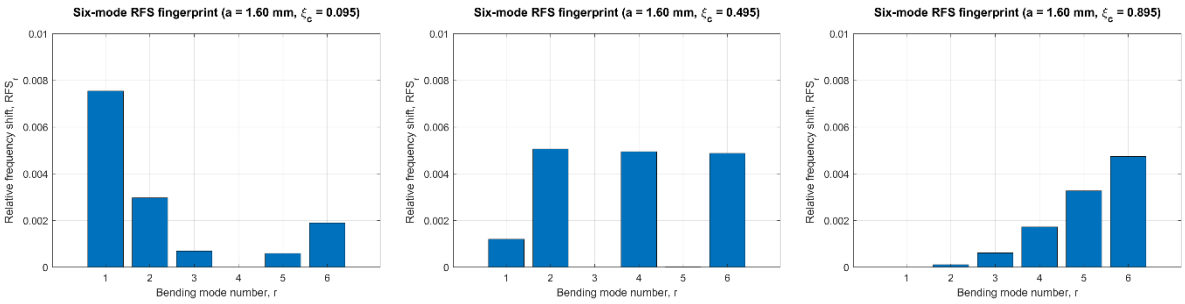

Figure 2. Example RFS "fingerprints" represented by the six-mode relative frequency shift vector for a fixed crack depth $a = 1.60$ mm at three crack locations: (a) $e = 10$ ($x_c = 0.095$ m, $\xi_c = 0.095$), (b) $e = 50$ ($x_c = 0.495$ m, $\xi_c = 0.495$), and (c) $e = 90$ ($x_c = 0.895$ m, $\xi_c = 0.895$). The changing bar patterns show that the multi-mode RFS signature varies with crack location, providing a compact fingerprint for the learning model. Source: Authors' work (generated in MATLAB).

Accordingly, each scenario i is represented by the input vector

$$\boldsymbol{X_i} = \left[\mathbf{RFS_1^{(i)}}, \mathbf{RFS_2^{(i)}}, \ldots, \mathbf{RFS_6^{(i)}}\right]^{\boldsymbol{T}} \in \mathbb{R}^{\mathbf{6}} \tag{15}$$

Stacking all scenarios yields the input matrix $\mathbf{X} \in \mathbb{R}^{6\times N}$, where each column corresponds to a single scenario. The first six bending modes were adopted as a compact and practically stable RFS representation. Lower and intermediate modes generally provide sufficient sensitivity to crack-induced stiffness changes while remaining more accessible and reliable for modal identification than very high modes. In contrast, higher modes may be more sensitive to measurement noise, boundary-condition uncertainties, and mode-identification errors, which can reduce the robustness of frequency-shift-based features in practical applications. Therefore, the six-mode input vector was selected to balance modal information content, numerical stability, and practical measurability. This choice also maintains compatibility with the external RFS consistency checks considered in this study.

Where f_r^H denotes the r −th natural frequency of the healthy beam, and $f_r^D(s)$ is the r −th natural frequency of the damaged beam in scenario s. These ratios provide compact global descriptors of crack-induced stiffness reduction.

2.6. Learning framework and training protocol

Based on the RFS features defined in Section 2.5, a supervised learning framework was developed to estimate crack location and crack depth from multi-mode vibration-derived inputs. Each simulated scenario is represented by a six-dimensional input vector constructed from the first six relative frequency shifts, while the outputs are defined in non-dimensional form as the normalized crack location and crack-depth ratio, i.e., $[\xi_c, \lambda]$, where $\xi_c = x_c/L$ and $\lambda = a/h$.

The learning strategy consists of two complementary stages. In the first stage, a global predictor is trained using the complete dataset to provide a coarse estimate of the crack state over the full cantilever span. In the second stage, segment-specific expert models are trained on nine partially overlapping beam segments using their corresponding subsets. During inference, the coarse prediction is used to identify the relevant segment, and the corresponding segment-wise model provides the refined output. This two-stage strategy follows the segmentation concept reported in [6].

For all models, training, validation, and test evaluation were conducted using the official Master Split defined in Section 2.4. The training subset was used for parameter learning, the

validation subset was used for model selection and monitoring during development, and the test subset was reserved exclusively for final performance reporting. Accordingly, all reported test metrics were obtained from held-out samples not used in either model fitting or validation.

In addition to the internal Train/Validation/Test evaluation, external literature-based RFS cases were considered only after model training as independent consistency checks to examine whether the learned mapping yields physically plausible predictions under published inputs. These external checks were not used for training, hyper parameter tuning, or model selection

3. Results and Discussion

3.1. Numerical behavior of RFS features

This subsection examines the numerical behavior of the relative frequency shift (RFS) features adopted as inputs to the learning model. As illustrated by the RFS distributions and example modal fingerprints in Fig. 1 and Fig. 2, the feature response varies with both the normalized crack location, ξ_c, and the crack depth ratio, $\lambda = a/h$, in a mode-dependent manner. In general, larger crack depths produce larger RFS magnitudes under the present numerical conditions, indicating increased stiffness loss as damage severity increases. At the same time, the variation across the beam span is not uniform, which shows that crack position also affects the modal sensitivity of the frequency-based descriptors.

These trends support the use of a multi-mode RFS representation rather than relying on a single frequency change alone. Different bending modes respond differently to the same crack scenario, and the combined six-mode RFS vector therefore provides a richer signature for separating the effects of crack location and crack depth within the controlled numerical dataset. In this sense, the observed feature patterns are physically consistent with crack-induced stiffness reduction and provide the basis for the supervised learning results reported in the following subsections.

Because the present dataset is generated in a controlled numerical environment, the RFS features used in this study are noise-free. In practical measurements, however, natural-frequency estimates may be affected by sensor noise, boundary-condition variability, excitation inconsistency, and environmental effects. Such disturbances may perturb the RFS values, especially when the crack-induced frequency shifts are small or when higher modes are considered. Therefore, the results reported here should be interpreted as a controlled numerical baseline rather than as direct evidence of field-ready robustness. A dedicated noise-sensitivity analysis and experimental validation are left for future work.

3.2. Evaluation metrics

Model performance is quantified using the mean absolute error (MAE) and the root mean square error (RMSE) for each predicted output $\mathcal{Y}$. Let N denote the number of evaluated samples, and let $\mathcal{Y}_i$ and $\hat{\mathcal{Y}}_i$ be the ground-truth and predicted values, respectively. The metrics are computed as

$$\mathbf{MAE}_{\mathcal{Y}} = \frac{1}{N}\sum_{i=1}^{N}\left|\mathcal{Y}_I - \hat{\mathcal{Y}}_I\right|, \qquad \mathbf{RMSE}_{\mathcal{Y}} = \sqrt{\frac{1}{N}\sum_{i=1}^{N}\left(\mathcal{Y}_I - \hat{\mathcal{Y}}_I\right)^2} \tag{16}$$

When applicable, RMSE is reported alongside MAE to provide complementary information on error dispersion. These metrics are used in the following subsections to evaluate the predictive performance of the proposed models.

 ISSN: 2617-5517 | **DOI**: https://doi.org/10.59746/byt32350

3.3. Baseline ANN performance

The baseline artificial neural network (ANN) was trained using the master split (Train/Validation/Test = 840/180/180) with min–max scaling computed from the training subset only. The outputs were the non-dimensional crack location ξ_c and crack-depth ratio λ, with reported errors also expressed in physical units (x in mm and a in mm). Table 1 summarizes the absolute-error metrics on the training, validation, and test subsets.

Table 1. Baseline ANN error metrics using the master split (RFS inputs, 6 modes). Source: Authors' work (generated in MATLAB).

Subset	MAE_x (mm)	RMSE_x (mm)	MAE_a (mm)	RMSE_a (mm)	MAE_λ	RMSE_λ
Train	2.329953	3.520619	0.023614	0.101059	0.004723	0.020212
Validation	2.877641	4.550011	0.024914	0.101215	0.004983	0.020243
Test	2.992080	4.559767	0.025055	0.084598	0.005011	0.016920

Table 1 shows that the baseline ANN provides a clear reference level of predictive performance under the adopted leakage-free evaluation protocol. On the held-out test subset, the model achieved a mean absolute error of 2.992 mm for crack location and 0.0251 mm for crack depth, corresponding to MAE values of 0.002992 in ξ_c and 0.005011 in λ. These results establish a controlled numerical benchmark for direct crack characterization from compact six-mode RFS inputs. This baseline is important because it provides the point of comparison against which the segmentation-based strategy is assessed in the following subsection.

3.4. Segmentation-based inference

A segmentation-based strategy was then evaluated, in which an overall ANN provides a coarse prediction used to gate each sample to the nearest segment center, followed by segment-level inference. The same official Master Split was retained to ensure a consistent and fair comparison with the baseline model. Table 2 reports the corresponding error metrics for the training, validation, and test subsets, while Table 3 summarizes the direct test-set comparison between the baseline and segmentation-based settings.

Table 2. Segmentation-based (gated) error metrics using the official Master Split (RFS inputs, 6 modes). Source: Authors' work (generated in MATLAB).

Subset	MAE_x (mm)	RMSE_x (mm)	MAE_a (mm)	RMSE_a (mm)	MAE_λ	RMSE_λ
Train	0.499408	1.734582	0.018822	0.107694	0.003764	0.021539
Validation	1.102354	2.243155	0.018808	0.094441	0.003762	0.018888
Test	1.245305	3.361693	0.021131	0.091397	0.004226	0.018279

Table 3. Test-set comparison between the baseline and segmentation-based settings under the same official Master Split. Source: Authors' work (generated in MATLAB).

Output	Metric	Baseline (Test)	Segmented (Test)	Relative change (%)
x (mm)	MAE	2.992080	1.245305	58.38
x (mm)	RMSE	4.559767	3.361693	26.27
a (mm)	MAE	0.025055	0.021131	15.66
a (mm)	RMSE	0.084598	0.091397	-8.04
λ	MAE	0.005011	0.004226	15.67
λ	RMSE	0.016920	0.018279	-8.03

The results show that the segmentation-based strategy improves predictive accuracy relative to the baseline model, especially for crack localization. On the held-out test subset, the mean absolute error of crack location was reduced from 2.992 mm to 1.245 mm, corresponding to an improvement of 58.38%, while the mean absolute error of crack depth decreased from 0.0251 mm to 0.0211 mm, corresponding to an improvement of 15.66%. By contrast, the RMSE of crack depth showed a slight increase, suggesting that a limited number of larger depth-prediction errors may still persist under the adopted gating strategy.

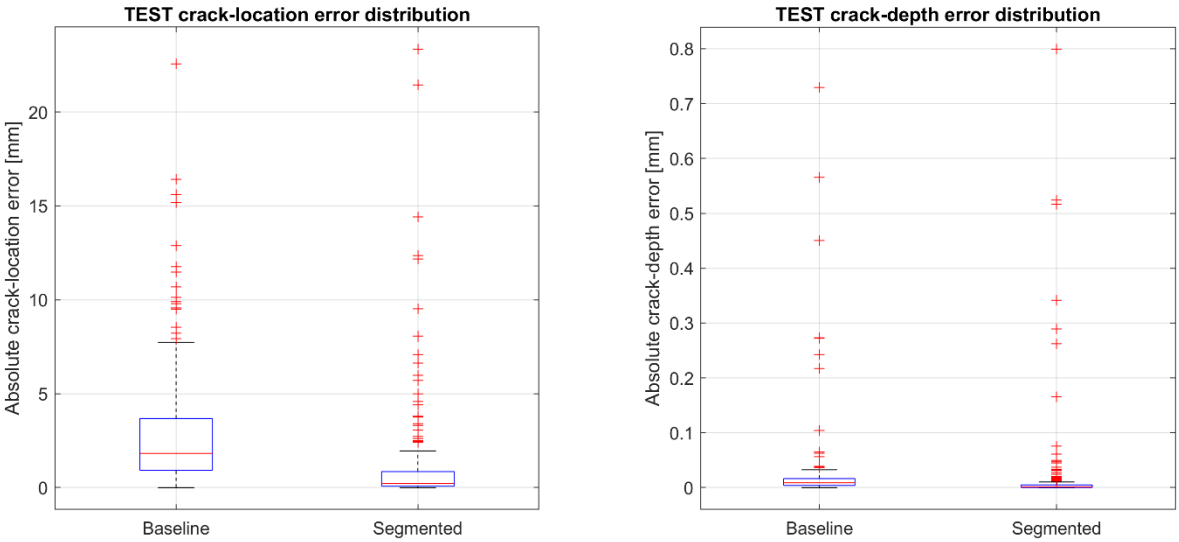

A b

Figure 3. Boxplot distribution of absolute test errors for the baseline and segmentation-based models: (a) crack-location error and (b) crack-depth error. The segmented model shows a lower central error distribution for crack localization, while the depth-error distribution includes a small number of large-error cases. Source: Authors' work (generated in MATLAB).

The error-distribution boxplots provide additional insight into the aggregated metrics reported in Table 3. For crack localization, the segmented model exhibits a lower central error range than the baseline model, indicating that the segmentation strategy reduces the typical position-prediction error across the test set. For crack depth, most errors remain small for both models; however, a limited number of larger errors are still present, which explains the slight increase in the depth RMSE despite the reduction in MAE.

This behavior is physically reasonable and consistent with the reduced mapping complexity introduced by segmentation. When the global crack-location range is partitioned into narrower sectors, each local model is trained over a more homogeneous subset of scenarios, which improves positional discrimination and reduces ambiguity in the input–output relationship. The benefit is more pronounced for crack location than for crack depth, because localization directly gains from restricting the admissible spatial search range, whereas depth estimation still depends on more subtle variations in the multi-mode RFS pattern within each segment. Accordingly, the segmentation-based strategy improves overall inference quality while preserving the same physics-based feature definition and the same leakage-free evaluation protocol.

From an interpretation perspective, the improvement in MAE indicates that the segmentation-based strategy reduces the typical prediction error across the test set, whereas the increase in depth RMSE suggests that a small number of larger depth errors still affect the error dispersion. Therefore, the segmented model should be viewed as primarily improving the central

tendency of the predictions, especially for crack localization, rather than uniformly reducing all error components.

3.5. Evaluation on selected numerical cases and out-of-grid samples

In addition to the global metrics on the official test split, the trained model was further evaluated on two complementary sets: (i) nine selected numerical samples and (ii) an out-of-grid set with three crack-depth levels not included in the training grid. These additional evaluations were introduced to provide a more detailed view of model behavior beyond the aggregated test-set metrics. The nine selected samples were chosen in a motivated manner to include locations aligned with the experimentally assessed cases used later for external consistency checks, while also spanning multiple crack-depth levels for illustrative per-sample reporting.

Table 4. Per-sample predictions for nine selected numerical cases (RFS inputs, 6 modes). Source: Authors' work (generated in MATLAB).

Sample ID	x_{true}(mm)	a_{true} (mm)	x_{pred} (mm)	a_{pred}(mm)	x_{error} (%)	a_{error}(%)
1	95.000	2.500	83.011	2.497704	1.1989	0.091840
2	315.000	1.250	313.143	1.252830	0.1857	0.226400
3	565.000	2.500	558.385	2.488156	0.6615	0.473760
4	125.000	2.500	116.402	2.470649	0.8598	1.174040
5	755.000	2.500	750.246	2.509994	0.4754	0.399760
6	315.000	0.800	316.380	0.838997	0.1380	4.874625
7	585.000	1.200	583.952	1.191640	0.1048	0.696667
8	395.000	1.200	398.404	1.206220	0.3404	0.518333
9	795.000	2.000	795.208	2.007706	0.0208	0.385300

Table 5. Aggregated errors for the selected-sample and out-of-grid numerical evaluations. Source: Authors' work (generated in MATLAB).

Dataset	N	MAE_x (mm)	$RMSE_x$ (mm)	MAE_a (mm)	$RMSE_a$ (mm)
Nine selected samples	9	4.428010	5.793600	0.013066	0.017650
Out-of-grid (all depths)	27	5.313243	6.461680	0.023942	0.032787

Table 6. Out-of-grid evaluation aggregated by crack depth level. Source: Authors' work (generated in MATLAB).

a_{true}(mm)	N	MAE_x (mm)	$RMSE_x$ (mm)	MAE_a (mm)	$RMSE_a$ (mm)
0.300	9.0	7.152092	7.722824	0.046714	0.052483
1.100	9.0	1.911814	2.339477	0.008734	0.011356
2.500	9.0	6.875824	7.755307	0.016379	0.018482

Table 4 shows that the model yields small errors for several of the selected numerical cases, while the aggregated results in Table 5 indicate that the overall prediction accuracy remains acceptable for both the selected-sample set and the out-of-grid set. At the same time, the out-of-

grid evaluation exhibits larger errors than the selected in-grid cases, which is expected because the queried crack depths are not restricted to the discrete levels used during training.

Table 6 further shows that prediction quality depends on the proximity of the queried depth to the depths represented during training. In particular, the intermediate depth level of 1.100 mm produced the smallest combined error, whereas the shallower 0.300 mm case and the deeper 2.500 mm case showed larger deviations. This trend indicates that the model performs more reliably for cases located near the interior of the learned crack-depth range, while predictions near the lower and upper boundaries are more sensitive to interpolation and near-boundary effects. Therefore, the out-of-grid results should be interpreted as a limited numerical consistency check around the prescribed training grid rather than as evidence of general extrapolation capability outside the studied crack-parameter domain.

3.6. External consistency check using literature-reported RFS inputs (Source [6])

To assess whether the trained model yields physically plausible estimates when driven by literature-reported inputs, five cases were extracted from Source [6] and used as direct inputs to the trained ANN. Because the original source reports eight-mode relative frequency shift (RFS) vectors, only Modes 1–6 were retained here to match the adopted input dimensionality of the present model. It is important to note that the damage variables are not defined and scaled identically in the two studies. In Source [6], damage severity is quantified using a displacement-based severity index, whereas the present study predicts crack depth through the physical crack-depth ratio. Therefore, the cross-study comparison is primarily meaningful for crack position, while the depth-related outputs are reported only for transparency and should not be interpreted as a direct one-to-one validation of crack-depth prediction.

Table 7. Literature-reported RFS input vectors adopted from Source [6] and used as model inputs in this study (Modes 1–6 only). Source: [6].

Case	x_{true}(mm)	a_{true}(mm)	RFS_1	RFS_2	RFS_3	RFS_4	RFS_5	RFS_6
Crack1	98	2.50	0.020610	0.007828	0.001629	0.000031	0.002070	0.005964
Crack2	310	1.25	0.001795	0.000660	0.002334	0.000600	0.000542	0.002654
Crack3	569	2.50	0.002382	0.017252	0.005019	0.009109	0.011488	0.002556
Crack4	126	2.50	0.023458	0.005550	0.000064	0.002581	0.008901	0.014021
Crack5	759	2.50	0.000288	0.005461	0.017336	0.017272	0.004422	0.000996

Table 8. Model predictions obtained by feeding the literature-reported RFS vectors into the trained ANN (6-mode RFS). Source: Authors' work (generated in MATLAB).

Case	xi_{pred}	$lambda_{pred}$	x_{pred} (mm)	a_{pred} (mm)
Crack1	0.086572	0.494032	86.571519	2.470159
Crack2	0.308888	0.241679	308.887611	1.208393
Crack3	0.573045	0.542314	573.045184	2.711570
Crack4	0.133870	0.522149	133.869730	2.610744
Crack5	0.726367	0.518481	726.367395	2.592404

Table 9. Cross-study comparison for the five literature cases. Position is comparable across studies (mm), whereas the severity measure reported in Source [6] is a displacement-based index and is not directly comparable to crack depth. Sources: [6] and this study.

Case	x_{true} (mm)	x_{pred} (mm) (this study)	Pos. error	Pos. error	a_{true} (mm)	a_{pred} (mm)	Depth error	Severity $\gamma(a)$)	Severity error

 ISSN: 2617-5517 | **DOI**: https://doi.org/10.59746/byt32350

	[6]		(%) (this study)	(%) [6]	[6]	(this study)	(%) (this study)	[6]	(%) [6]
Crack1	98	86.571519	1.1428	0.00	2.50	2.470159	1.1936	0.0275	0.13
Crack2	310	308.887611	0.1112	0.00	1.25	1.208393	3.3285	0.0054	0.03
Crack3	569	573.045184	0.4045	0.10	2.50	2.711570	8.4628	0.0343	0.81
Crack4	126	133.869730	0.7870	0.00	2.50	2.610744	4.4298	0.0343	0.81
Crack5	759	726.367395	3.2633	0.10	2.50	2.592404	3.6962	0.0343	0.81

The results show that the trained model produces position estimates that remain physically plausible when driven by literature-reported RFS inputs. In particular, the inferred crack locations fall within the beam span and exhibit small position errors relative to the reference values reported in Source [6]. This outcome supports the consistency of the learned mapping beyond the internally generated numerical dataset. At the same time, the depth estimates should not be interpreted as direct replications of the severity values reported in Source [6], because the two studies do not use equivalent damage-severity definitions. Accordingly, this subsection is best interpreted as an external consistency check for the position-related behavior of the model rather than as a strict one-to-one validation of all output quantities.

3.7. External position-only consistency check using experimentally reported RFS inputs (Source [18])

The following complementary check was conducted using an independently reported experimental dataset from Source [18]. The dataset provides relative frequency shift (RFS) vectors together with a non-dimensional crack location (generated position). For completeness, the corresponding crack depths for the four experimental cases were taken from the publicly available Mendeley Data dataset (https://doi.org/10.17632/ t8bscbsv5d.1), which is provided by an author of Source [18]. However, the present comparison remains position-oriented because the externally reported study focuses primarily on crack-location assessment rather than direct crack-depth validation.

Table 10. Experimentally reported RFS inputs adopted from Source [18] (Table 8) and used as model inputs in this study (Modes 1–6 only). Source of RFS inputs: Source [18], Table 8; model inference: this study.

Case	Generated position, ξ	RFS_1	RFS_2	RFS_3	RFS_4	RFS_5	RFS_6
Crack1	0.310	0.0012	0.0007	0.0018	0.0005	0.0004	0.0019
Crack2	0.587	0.0002	0.0044	0.0020	0.0015	0.0039	0.0022
Crack3	0.395	0.0020	0.0028	0.0026	0.0006	0.0046	0.0001
Crack4	0.795	0.0000	0.0020	0.0103	0.0135	0.0071	0.0006

Table 11. Position-only comparison using experimentally reported cases from Source [18] (Table 8). Crack depth is not assessed in this table because Source [18] focuses on position-related outcomes. Source of reference positions: Source [18], Table 8; model inference: this study.

Case	ξ_{true} (Source [18])	ξ_{pred}(This study)	Error % (This study)	Error % (Source [18])
Crack1	0.310	0.316380	0.638	0.52
Crack2	0.587	0.583952	0.305	0.90
Crack3	0.395	0.398404	0.340	1.90

Crack4	0.795	0.795208	0.021	1.18

In this study, the RFS vectors reported in Source [18] were used as direct inputs to the trained model after retaining Modes 1–6 only to match the adopted six-mode feature definition. Tables 10 and 11 report the adopted RFS inputs and the corresponding position estimates, respectively, enabling a direct comparison against the reference generated positions reported in Source [18]. The results show that the trained model yields small position errors for all four external cases, which supports the positional consistency of the learned mapping when driven by experimentally reported RFS inputs.

At the same time, this agreement should be interpreted as a qualitative consistency check rather than as a strict one-to-one experimental validation. Experimental conditions, boundary compliance, sensor placement, and noise characteristics may differ from the controlled numerical conditions adopted in the present study. Accordingly, this subsection provides additional evidence that the trained model can produce physically plausible crack-location estimates under published external inputs, while full experimental validation remains beyond the scope of the present numerical baseline.

4. Conclusion

This study presented a fully numerical MATLAB-based framework for vibration-based crack characterization in a cantilever beam using compact multi-mode relative frequency shift (RFS) features. A one-dimensional Euler–Bernoulli finite-element formulation with an element-level crack representation and static condensation was used to generate a controlled labelled dataset for supervised learning. Under the adopted leakage-free Master Split, the baseline artificial neural network (ANN) achieved a test-set mean absolute error of 2.992 mm for crack location and 0.0251 mm for crack depth. A segmentation-based coarse-to-fine inference strategy further improved the reported accuracy under the same official split. In particular, the test mean absolute error of crack location was reduced from 2.992 mm to 1.245 mm, corresponding to an improvement of 58.38%, while the crack-depth mean absolute error was reduced from 0.0251 mm to 0.0211 mm, corresponding to an improvement of 15.66%. These results indicate that segment-wise inference can improve RFS-based prediction, especially for crack localization, when implemented within a unified and leakage-free evaluation protocol. Additional evaluations on selected numerical cases, out-of-grid crack-depth levels, and literature-reported RFS inputs further supported the physical plausibility of the learned mapping within the scope of the present study. At the same time, these external cases were interpreted as consistency checks rather than as direct one-to-one validation whenever the source definitions were not strictly equivalent to the crack-depth representation adopted here. A key limitation of this study is that the main training and testing process is based on a fully numerical dataset generated for a single cantilever-beam configuration. Although literature-reported RFS inputs were used as external consistency checks, no dedicated experimental dataset was generated within this work for full experimental validation. Therefore, the reported results should be interpreted as a controlled numerical baseline, and further validation is required before extending the framework to broader structural configurations or field conditions. The main contribution of this work is the development of a reproducible leakage-free segmentation-based ANN framework for simultaneous crack localization and depth estimation from compact RFS inputs. From a practical perspective, the proposed framework provides a controlled numerical baseline that can support the development of vibration-based crack-identification tools using a small number of frequency-derived features. The leakage-free evaluation protocol is also practically relevant because it provides a transparent basis for comparing baseline and segmented

learning strategies without split-induced bias. However, the present findings should be interpreted within the limits of a controlled numerical and noise-free setting for a single cantilever-beam configuration and a prescribed crack-parameter grid. Real-world deployment would require further assessment under measurement noise, boundary-condition variability, environmental influences, and dedicated experimental validation. Accordingly, the reported accuracy should be regarded as a reproducible numerical baseline rather than as a direct claim of field-ready robustness. Future work should therefore extend the framework toward noisy conditions, broader structural scenarios, and experimental validation to assess practical robustness under real measurement conditions.

Author Contributions: All authors contributed equally to the conceptualization, methodology, analysis, writing, and revision of this manuscript. All authors read and approved the final version of the manuscript.
Conflicts of Interest: The authors declare that they have no conflicts of interest.
Ethical Approval: This study did not involve human or animal subjects, and ethical approval was not required.
Data Availability Statements: The data supporting the findings of this study are available from Mohammad Majeed upon reasonable request.

REFERENCES

[1] A. A. S. R. de Sousa, J. da Silva Coelho, M. R. Machado, and M. Dutkiewicz, "Multiclass Supervised Machine Learning Algorithms Applied to Damage and Assessment Using Beam Dynamic Response," *J. Vib. Eng. Technol.*, vol. 11, no. 6, pp. 2709–2731, Sep. 2023, doi: 10.1007/s42417-023-01072-7.

[2] D. M. Ashigbi, M. N. Sackey, Y. A. K. Fiagbe, and J. Quaye-Ballard, "Vibration response based crack diagnosis in beam-like structures using fuzzy inference system," *Sci. African*, vol. 14, p. e01051, Nov. 2021, doi: 10.1016/j.sciaf.2021.e01051.

[3] R. Katam, V. D. K. Pasupuleti, and P. Kalapatapu, "Machine learning-driven structural health monitoring: STFT-based feature extraction for damage detection," *Structures*, vol. 78, no. 3, p. 109244, Aug. 2025, doi: 10.1016/j.istruc.2025.109244.

[4] M. Parziale, P. H. Silva, M. Giglio, and F. Cadini, "Explainability of convolutional neural networks for damage diagnosis using transmissibility functions," *Structures*, vol. 69, no. January, p. 107583, Nov. 2024, doi: 10.1016/j.istruc.2024.107583.

[5] M. Moravvej and M. El-Badry, "Reference-Free Vibration-Based Damage Identification Techniques for Bridge Structural Health Monitoring—A Critical Review and Perspective," *Sensors*, vol. 24, no. 3, p. 876, Jan. 2024, doi: 10.3390/s24030876.

[6] N. Gillich *et al.*, "Beam Damage Assessment Using Natural Frequency Shift and Machine Learning," *Sensors*, vol. 22, no. 3, p. 1118, Feb. 2022, doi: 10.3390/s22031118.

[7] S. K. Gupta and S. Das, "Multiple Damage Identification in a Beam Using Artificial Neural Network-Based Modified Mode Shape Curvature," *Arab. J. Sci. Eng.*, vol. 47, no. 4, pp. 4849–4864, Apr. 2022, doi: 10.1007/s13369-021-06267-2.

[8] M.-H. Tran *et al.*, "A novel approach for identifying structural damage in beams with diverse boundary conditions using modal strain energy method combined with convolutional neural networks," *Structures*, vol. 80, no. September, p. 110062, Oct. 2025, doi: 10.1016/j.istruc.2025.110062.

[9] S. M. H. Pooya and A. Massumi, "A novel and efficient method for damage detection in beam-like structures solely based on damaged structure data and using mode shape curvature estimation," *Appl. Math. Model.*, vol. 91, pp. 670–694, Mar. 2021, doi: 10.1016/j.apm.2020.09.012.

[10] Y. Zhang, Z. Xu, G. Li, and C. Xin, "An enhanced hybrid method for structural damage detection using DOG multi-scale analysis and adaptive fuzzy clustering," *Eng. Fail. Anal.*, vol. 179, no. April, p. 109785, Sep. 2025, doi: 10.1016/j.engfailanal.2025.109785.

[11] P. Saha and M. Yang, "A Neural Network Approach to Estimate the Frequency of a Cantilever Beam with Random Multiple Damages," *Sensors*, vol. 23, no. 18, p. 7867, Sep. 2023, doi: 10.3390/s23187867.

[12] S. J. Seyed Hakim, M. J. Irwan, M. H. W. Ibrahim, and S. S. Ayop, "Structural damage identification employing hybrid intelligence using artificial neural networks and vibration-based methods," *J. Appl. Res. Technol.*, vol. 20, no. 2, pp. 221–236, May 2022, doi: 10.22201/icat.24486736e.2022.20.2.1233.

[13] M. Torzoni, M. Tezzele, S. Mariani, A. Manzoni, and K. E. Willcox, "A digital twin framework for civil engineering structures," *Comput. Methods Appl. Mech. Eng.*, vol. 418, no. PB, p. 116584, Jan. 2024, doi: 10.1016/j.cma.2023.116584.

[14] X. Zhang and Y. Lu, "A novel wavelet energy feature for damage identification with a digital twin considering measurement uncertainties," *J. Struct. Integr. Maint.*, vol. 10, no. 1, Jan. 2025, doi: 10.1080/24705314.2024.2440830.

[15] R. S. Battu, K. Agathos, J. M. Londoño Monsalve, K. Worden, and E. Papatheou, "Combining transfer learning and numerical modelling to deal with the lack of training data in data-based SHM," *J. Sound Vib.*, vol. 595, no. December 2023, p. 118710, Jan. 2025, doi: 10.1016/j.jsv.2024.118710.

[16] A. S. Yehia, D. K. Harris, and A. A. Aljundi, "What lies within: Utilizing graph neural networks for subsurface detection in finite element simulations," *Eng. Struct.*, vol. 341, no. June, p. 120842, Oct. 2025, doi: 10.1016/j.engstruct.2025.120842.

[17] M. Torzoni, A. Manzoni, and S. Mariani, "A multi-fidelity surrogate model for structural health monitoring exploiting model order reduction and artificial neural networks," *Mech. Syst. Signal Process.*, vol. 197, no. November 2022, p. 110376, Aug. 2023, doi: 10.1016/j.ymssp.2023.110376.

[18] C. V. Rusu, G.-R. Gillich, C. Tufisi, N. Gillich, T. H. Bui, and C. Ionut, "A Stacked Neural Network Model for Damage Localization," *Sensors*, vol. 24, no. 21, p. 7019, Oct. 2024, doi: 10.3390/s24217019.

[19] J. Fish and T. Belytschko, *A First Course in Finite Elements*. Wiley, 2007. doi: 10.1002/9780470510858.

[20] D. Imamović and M. Skrinar, "Static bending analysis of a transversely cracked strip tapered footing on a two-parameter soil using a new beam finite element," *Contin. Mech. Thermodyn.*, vol. 36, no. 3, pp. 571–584, May 2024, doi: 10.1007/s00161-024-01283-7.

[21] A.-T. Aman, C. Tufisi, G.-R. Gillich, and Z. I. Praisach, "Detection of transverse cracks in steel beams using damage location coefficients and artificial neural networks," *Vibroengineering Procedia*, vol. 50, pp. 42–48, Sep. 2023, doi: 10.21595/vp.2023.23432.